RESEARCH OUTPUTS / RÉSULTATS DE RECHERCHE

Multilevel Hollow Phenolic Resin Nanoreactors with Precise Metal Nanoparticles Spatial Location toward Promising Heterogeneous Hydrogenations

Pi, Yutong; Ma, Yanfu; Wang, Xinyao; Price, Cameron Alexander Hurd; Li, Haitao; Liu, Qinglong; Wang, Liwei; Chen, Hongyu; Hou, Guangjin; Su, Bao Lian; Liu, Jian

Link to publication

Multilevel Hollow Phenolic Resin Nanoreactors with Precise Metal Nanoparticles Spatial Location toward Promising Heterogeneous Hydrogenations

Yutong Pi, Yanfu Ma, Xinyao Wang, Cameron-Alexander Hurd Price, Haitao Li, Qinglong Liu, Liwei Wang, Hongyu Chen, Guangjin Hou, Bao-Lian Su,* and Jian Liu*

Hollow nanostructures with fascinating properties have inspired numerous interests in broad research fields. Cell-mimicking complex hollow architectures with precise active components distributions are particularly important, while their synthesis remains highly challenging. Herein, a "top-down" chemical surgery strategy is introduced to engrave the 3-aminophenol formaldehyde resin (APF) spheres at nanoscale. Undergoing the cleavage of (Ar) C−N bonds with ethanol as chemical scissors and subsequent repolymerization process, the Solid APF transform to multilevel hollow architecture with precise nanospatial distribution of organic functional groups (e.g., hydroxymethyl and amine). The transformation is tracked by electron microscopy and solid-state nuclear magnetic resonance techniques, the category and dosage of alcohol are pivotal for constructing multilevel hollow structures. Moreover, it is demonstrated the evolution of nanostructures accompanied with unique organic microenvironments is able to accurately confine multiple gold (Au) nanoparticles, leading to the formation of pomegranate-like particles. Through selectively depositing palladium (Pd) nanoparticles onto the outer shell, bimetallic Au@APF@Pd catalysts are formed, which exhibit excellent hydrogenation performance with turnover frequency (TOF) value up to 11257 h^{-1}. This work provides an effective method for precisely manipulating the nanostructure and composition of polymers at nanoscale and sheds light on the design of catalysts with precise spatial active components.

1. Introduction

Cells are a natural, soft matter with multilevel hollow structures and precisely located functional groups. So far, the mimicking of the construction of cells in artificial organelles, or so-called nanoreactors, is mainly focused on inorganic materials such as metal oxides, it still remains challenging to design organic macromoleculars with multilevel hollow structures due to the limitations of polymer chemistry and nanochemistry. As one of the traditional polymers, following Baekeland's pioneering efforts in 1907, phenolic resins have been and are still being applied widely in various fields such as adhesives, insulation materials for heat and sound, paints, and structural materials, because of their unique properties (good adhesiveness, thermal stability, flame retardance, etc.).[1–3] Among most of the nanostructured polymers, the tailorable chemical structure, nanoarchitecture and easy functionalization for nanostructured phenolic resins, endow them with varied catalytic[4]

Y. Pi, Y. Ma, X. Wang, H. Li, Q. Liu, L. Wang, H. Chen, G. Hou, J. Liu
State Key Laboratory of Catalysis
Dalian Institute of Chemical Physics
Chinese Academy of Sciences
457 Zhongshan Road, Dalian 116023, China
E-mail: jian.liu@surrey.ac.uk
Y. Pi, X. Wang, L. Wang, H. Chen
University of Chinese Academy of Sciences
19A Yuquan Rd, Shijingshan District, Beijing 100049, China
C.-A. H. Price
Department of Chemical Engineering and Analytical Science
University of Manchester
Oxford Rd, Manchester M13 9PL, UK

C.-A. H. Price
The University of Manchester at Harwell
Diamond Light Source
Didcot, Oxfordshire OX11 0DE, UK
C.-A. H. Price
UK Catalysis Hub, Research Complex at Harwell
Rutherford Appleton Labs
Harwell campus, Didcot, Oxfordshire OX11 0FA, UK
C.-A. H. Price, J. Liu
DICP-Surrey Joint Centre for Future Materials
Department of Chemical and Process Engineering
University of Surrey
Guildford, Surrey GU2 7XH, UK
B.-L. Su
Laboratory of Inorganic Materials Chemistry
University of Namur
61, rue de Bruxelles, Namur 5000, Belgium
E-mail: bao-lian.su@unamur.be

**ADVANCED
SCIENCE NEWS**

www.advancedsciencenews.com

**ADVANCED
MATERIALS**

www.advmat.de

and biomedical applications (such as in vivo bioimaging, drug/ gene delivery and cell targeting[5–8]). In addition, carbon materials with versatile micro/nanostructures derived from phenolic resins can be used as absorbents, catalyst supports, and electrode materials in energy storage and conversion.[9–11] In various designs of nanostructured materials, the multilevel hollow nanoreactor makes it a focus of attention. The key structural and functional features relevant to these special hollow structures are as follows: 1) the multilevel interior structures are favorable to expose more accessible active sites.[12,13] 2) the built-in cavity and nanopores provide spatial environment for the location of metal nanoparticles and are capable of protecting the isolated metal from aggregation.[14]

Over the last decades, much effort has been paid to developing advanced synthetic strategies of various intricate nanostructured polymers. For example, Li et al. reported a programmable shear-induced dynamic assembly method to fabricate polydopamine nanosphere with gradient-pore structure.[12] Similarly, polydopamine nanoparticles with multi-shelled hollow architectures could be obtained by the lamellar micelle spiral self-assembly strategy.[15] Up to ten kinds of hollow structured covalent organic frameworks can also be successfully achieved through an efficient strategy of amorphous-to-crystalline transformation.[16] Specific to the controllable synthesis of nanostructured phenolic resins, two general paradigms were proposed; bottom-up and top-down. Among them, bottom-up self-assembling approaches based on the different polymerization mechanisms have gained great attention.[17,18] For example, monodispersed resorcinol formaldehyde resin (RF) and 3-aminophenol formaldehyde resin (APF) nanospheres with tailorable particle size from 100 to 1000 nm can be obtained by the extension of Stöber method.[19,20] With the assistance of soft templates (such as emulsion droplets, micelles, or vesicles), the mesoporous phenolic resins present tunable and uniform sizes.[21–24] Notwithstanding the above progress in the synthetic methodology, the nanostructured phenolic resins reported so far usually show a simple solid or mesoporous configuration. Most recently, in order to increase the complexity of nanostructured phenolic resins, the top-down approaches are becoming increasingly explored.[25] With the treatment of acetone, parts of APF can be dissolved, leading to the formation of multi-shelled hollow and intricate concave structured APF nanoparticles.[26,27] Similarly, Yin et al. reported the dissolution and regrowth process to construct hollow RF nanoshells.[28] Although in these cases, the complexity and diversity of nanostructured phenolic resins have been expanded, nanoengineering them with finely controlled hollow multilevel interior structures at the nanoscale has only reported limited success. In addition, the limited synthetic strategies underscore the challenge in designing polymers with accurately located functional groups. The construction of nanostructured materials with controllable composition, structure and functional groups is

important in cascade catalysis and artificial photosynthesis, which can even act as artificial organelles and nanoreactors to mimic the functionalities of enzymes and cells.[29–32]

The hydrogenation reactions are one of the most challenging catalytic reactions and play an important role in the production of both bulk and fine chemicals.[33] Heterogeneous catalysts, especially those supported metal catalysts, are at the heart of hydrogenations. To optimize their catalytic efficiency and selectivity, the structural complexity for supported metal catalysts is often well-designed, including controlling the size and composition of the supported metals, developing a specific microenvironment around the active species, spatially positioning single metal or multiple nanoparticles, and so on.[34] Among them, spatially localizing single or multiple metal nanoparticles is perhaps the most difficult and cutting edge of designing supported metal catalysts. Materials that succeed in this are catalysts that can provide molecular sieving capability to realize size-selective reactions, protect metal nanoparticles against agglomerating, and even enable effective cascade catalysis.[35,36] Despite the great success in architecting specific catalysts with precise spatial position of metal nanoparticles, the obtained metal nanoparticles often possess a single composition, and it is difficult to precisely position multi-type nanoparticles, because of the deficiency in effective methods and suitable supports. In addition, the development of highly active hydrogenation catalysts also remains a great challenge. Pd-based catalysts were employed as the most promising option for liquid hydrogenations because of their moderate reactivity toward H_2.[37] Many catalysts, including Ni-CeO$_{2-x}$/Pd,[38] Pd$_1$/BP,[39] Pd NCs@NCM,[40] and Pd/ZnO@C,[41] have been utilized for styrene and phenylacetylene hydrogenations, but gave rather low TOFs. Consequently, the construction of a new kind of catalyst with not only precise metal nanoparticle spatial location, but efficient catalytic performance has become a desirable target.

Herein, we report a form of nanoscale chemical surgery on APF to accurately tailor its nanostructure and chemical composition by using ethanol as the chemical scalpel (**Scheme 1**). Ethanol cleaves the chemical bonds ((Ar)C−N bonds), leading to the dissolution of oligomers. Following the repolymerization process, the Solid APF transforms into multilevel hollow structures (hollow cavities, mesoporous interior, and outer shell) with precise nanospatial distribution of organic functional groups (e.g., hydroxymethyl and amine). By regulation of the type and dosage of alcohol, a series of nanostructured APF particles are obtained. The unique multilevel hollow structures and their organic microenvironments are pivotal for the construction of novel nanomaterials with precise spatial location of metal nanoparticles, Au nanoparticles (NPs) fully embedded within one APF resin and PdNPs selectively deposited on their outer shell, which shows remarkable catalytic hydrogenation performance.

2. Results and Discussion

2.1. The Nanostructures Characterizations of Chemical Surgery Process

Solid APF with inhomogeneous chemical structure can be obtained in a short time, because of its typical formation

B.-L. Su
State Key Laboratory of Advanced Technology for Materials Synthesis and Processing
Wuhan University of Technology
122 Luoshi Road, Wuhan 430070, China
J. Liu
School of Chemistry and Chemical Engineering
Inner Mongolia University
235 West University Street, Hohhot 010021, China
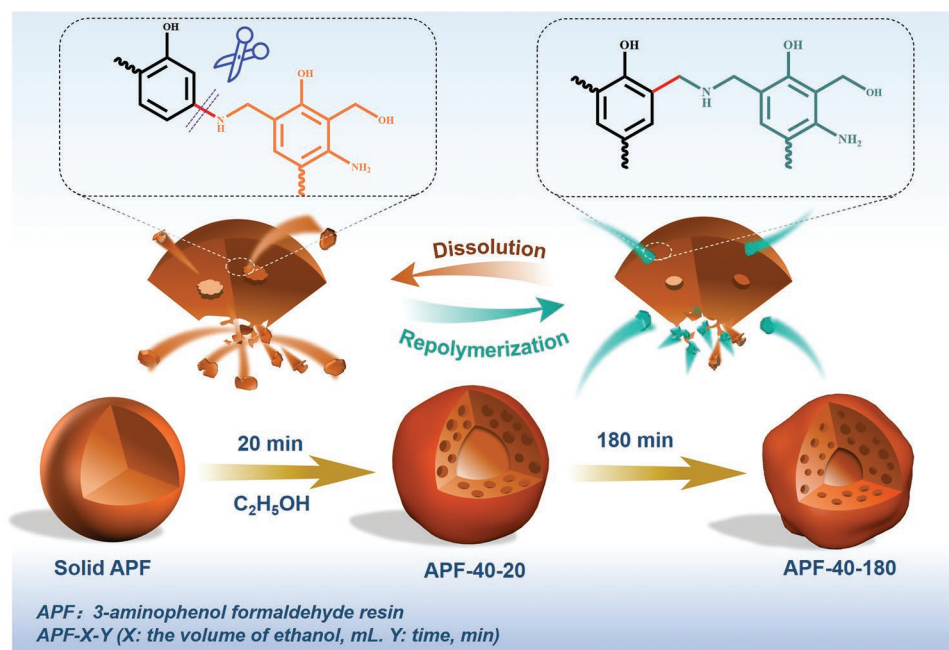
Scheme 1. Schematic illustration of the formation of nanostructured APF and the dissolution and repolymerization processes.

mechanism.[42] As shown in Figure S1 (Supporting Information), in the initial step, hydroxymethyl/benzoxazine derivatives were generated by addition reaction of phenol-aldehyde and amino-aldehyde in the emulsion droplets and further condensation reaction was completed in an extremely short time to form oligomers. Subsequently, the remaining substrate molecules tended to react with oligomers at the surface of the emulsion droplets due to the steric effect, thus forming the APF spheres with inhomogeneity in the core and shell composition. With continuous growth and crosslinking, it was found that the closer to the outer surface of APF spheres, the higher the polymerization degree (Figure S2, Supporting Information). Therefore, the Solid APF synthesized in this way was able to provide the corresponding oligomer for ethanol tailoring, which shows a promising opportunity for the construction of unique multilevel hollow structures. Then, ethanol (40 mL) was introduced as the chemical scalpel to initiate the dissolution and repolymerization processes to fabricate the nanostructured APF resins. The morphology of these samples with the assistance of ethanol after polymerization was characterized by transmission electron microscopy (TEM), scanning transmission electron microscopy (STEM), high resolution scanning electron microscopy (HRSEM), and energy-dispersive (EDX) mapping as shown in **Figure 1**. As can be seen in Figure 1a,b, when the dissolving time was 20 min, there is an immediately noticeable shape transformation of the resin solid spheres toward hollow and imperceptible curved structure. This is because ethanol is capable of cleaving APF with low cross-linking degree.[26] In order to characterize the degree of dissolution and the geometry of the partially dissolved APF, a parameter, namely, ζ = d/s, the size ratio of the cavity diameter (d) to the shell thickness (s) was defined. The meaning of these size ratios and the corresponding structural information are shown in Table S1 (Supporting Information). The size ratio for APF-40-20 was 4.2,

indicating a relatively high dissolving degree. When the time was extended to 180 min, the concave structure became more obvious. Hollow cavities, mesoporous interior, and ≈30 nm outer shell could be observed (Figure 1d,e). It should be noted that, compared with APF-40-20, the diameter of the interior cavity and the volume of mesopores of APF-40-180 became smaller, and the d/s value reduced to 2.0, which is due to the repolymerization of dissolved oligomer chains on the APF spheres. The elemental mapping was carried out as shown in Figure 1c,f. Both the APF-40-20 and APF-40-180 samples showed the evenly distributed C, O, and N elements within the particles. The obtained APF-40-180 possessed regular morphology, which is conducive to the formation of a uniform 3D periodic structure, and presents close-packed hexagonal planes arranged along the (111) direction (Figure 1g,h). Figure 1h clearly showed that this organization is not a localized phenomenon but affects the entire sample, and presents the right pink structural color at the same time, which stems from interference and reflection of light by periodical variation dielectric contrast or refractive index within the structure (insets of Figure 1h). In addition, originating from the same APF nanoparticles, Solid APF, APF-40-20 and APF-40-180 showed similar specific surface areas (Figure S3, Supporting Information). While the APF synthesized by water (30 mL)/ethanol (40 mL) binary solvent mixture exhibited spherical and solid structure, instead of curved and hollow structures, verifying that the moment of ethanol addition is an important step for the preparation of hollow multilevel APF (Figure S4, Supporting Information).

2.2. The Chemical Composition of Chemical Surgery Process

The solid-state nuclear magnetic resonance (ssNMR) was conducted to understand the ethanol action in the dissolution and
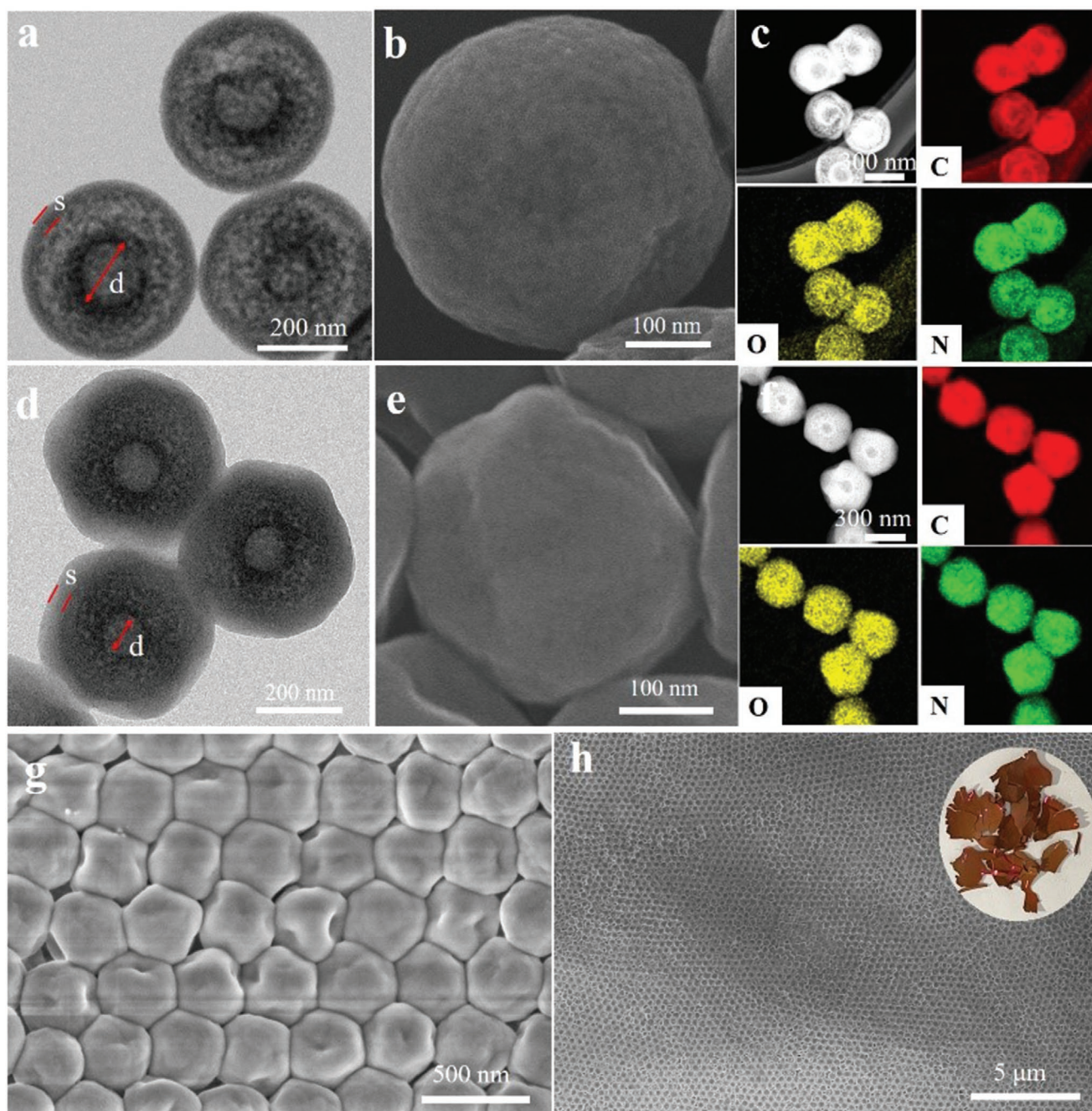
**ADVANCED
SCIENCE NEWS**

www.advancedsciencenews.com

**ADVANCED
MATERIALS**

www.advmat.de

Figure 1. Morphological and mesostructural characterizations of 1) APF-40-20: a) TEM image, b) high magnification HRSEM image, c) dark-field STEM image, and EDX mapping (C, O, N) results. 2) APF-40-180: d) TEM image, e) high magnification HRSEM image, f) dark-field STEM image, and EDX mapping (C, O, N) results, g) high magnification and h) low magnification HRSEM images of self-assembled APF-40-180 (inset, physical photography of the as-synthesized APF-40-180).

repolymerization of APF. **Figure 2**a showed the ^{13}C CP/MAS NMR spectrum of pure 3-aminophenol (3-AP). Obviously, the six lines among 106 and 158 ppm belong to the carbons in the benzene ring of 3-AP.[43,44] The ^{13}C CP/MAS NMR spectrum of Solid APF was shown in Figure 2b, the result was significantly different from pure 3-AP. Using DMFIT software fitting, the strong peaks at 106, 111, 118, 131, 146, and 158 ppm were almost the same as the carbon in 3-AP, which can be attributed to the

carbons in the benzene rings of APF, and those signals with chemical shifts in the ranges of ≈0–60 ppm belonged to the alkylated carbons. After ethanol treatment, the chemical shifts for all those peaks were almost the same, except for the relative intensives (Figure 2c). Among them, a stepwise decrease in the peak intensity of 146 ppm was observed. The calculated relative peak areas of 146 ppm were shown in Figure S5 (Supporting Information). It can be seen clearly that the peak area
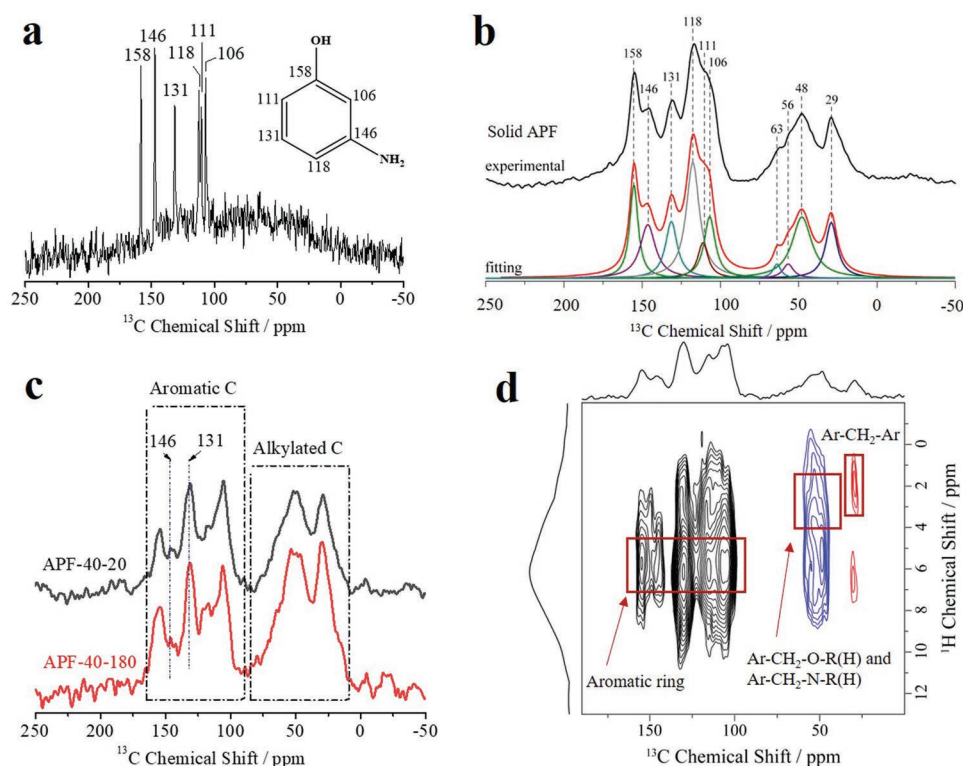
2205153 (4 of 11)

Figure 2. ^{13}C CP/MAS NMR spectra of a) 3-AP, b) Solid APF. Experimental NMR spectra are shown in upper traces, while the simulated spectra are shown in lower traces. c) ^{13}C CP/MAS NMR spectra of APF-40-20 and APF-40-180. d) 2D ^{1}H-^{13}C NMR spectrum of APF-40-180.

decreased from 15.39% to 8.14% after adding ethanol, and further decreased to 5.04% by prolonging the time to 180 min. Meanwhile, the relative peak areas for 113 ppm displayed an inverse trend (from 13.47% to 26.65%). This phenomenon demonstrated that ethanol breaks down the chemical bonds between the aromatic C and N to form the hydroxymethyl derivatives and porous APF. On the other hand, after adding the ethanol, the relative intensity of the signals of the aromatic C and alkylated C tended to decrease with prolonging the dissolving time. The ratio of peak area of aromatic C and alkylated C increased from 0.33 to 1.23 (Figure S6, Supporting Information), which may be due to that the oligomer with a lower degree of polymerization was easier to be dissolved by ethanol, and higher degrees of oligomer polymerization were still present in the APF.[28] The 2D ^{1}H-^{13}C heteronuclear correlation experiment can provide direct evidence for identifying the structure of the APF-40-180 (Figure 2d). The aromatic ring could be well defined with the correlation of peaks at $\delta(^1$H) ≈5–7 ppm and $\delta(^{13}$C) at ≈100–160 ppm. The blue lines marked in this spectrum correspond to Ar−CH$_2$−O−R(H) and Ar−CH$_2$−N−R(H) groups. Meanwhile, the correlation peak of $\delta(^1$H) at ≈0.5–3.5 ppm and $\delta(^{13}$C) at ≈28 to 32 ppm belong to Ar−CH$_2$−Ar group.

Fourier transform infrared (FTIR) spectra were also carried out to investigate the structural details of the obtained materials and the reaction mechanism of ethanol and APF (Figure S7a, Supporting Information). Both the Solid APF and the APF-40-180 showed the same spectrum but with different intensities. Typically, the absorption bands at 3376 cm^{-1} are assigned to O−H stretching vibrations, which may relate to OH■■■N,

OH■■■O, and OH■■■π hydrogen bonding.[45–47] The peak at 2925 cm^{-1} is attributed to −CH$_2$ stretching.[20] The absorbance peak at 1621 cm^{-1} is due to the C=C stretching in the aromatic rings in the obtained APF spheres.[48] Bands observed at 1592 cm^{-1} can be assigned to Ar−NH$_2$ stretching vibrations, 1511 cm^{-1} to −NH stretching, 1440 cm^{-1} to −CH stretching, 1384 cm^{-1} to (Ar)C−H stretching, 1305 cm^{-1} to (Ar)C−N stretching, 1241 cm^{-1} to C−N stretching, 1199 cm^{-1} to −O−C stretching and 1114 cm^{-1} to C−O−C stretching.[20] In addition, the FTIR for the etched oligomers of the APF-40-180 was also shown for comparison. Peak for C−O (1045 cm^{-1}) originated from ethanol. Interestingly, compared with APF-40-180, the etched oligomers of APF-40-180 showed negligible peak intensity of −C−O−C, C−N, and N−H, which belong to the oligomers' chains, suggesting that the ethanol cleaved some chemical bonds belonging to the low crosslinking degree APF and the remaining APF contains relatively more branches. The phenomena observed above are consistent with ^{13}C-ssNMR results. Besides, the Matrix-Assisted Laser Desorption/Ionization Time of Flight mass spectrometry was used to analyze the composition of these dissolved oligomers (Figure S7b, Supporting Information). Obviously, the molecular weight of the dissolved oligomers was below 400, meaning that the inner part of Solid APF was mainly composed of shorter chain oligomers, which are easily etched away by ethanol.[28] At the same time, with the extension of reaction time, the yield of resin showed a trend of first decreasing and then increasing (Figure S8, Supporting Information). The mechanism of alcoholic-assisted dissolution and regrowth was confirmed from another aspect.
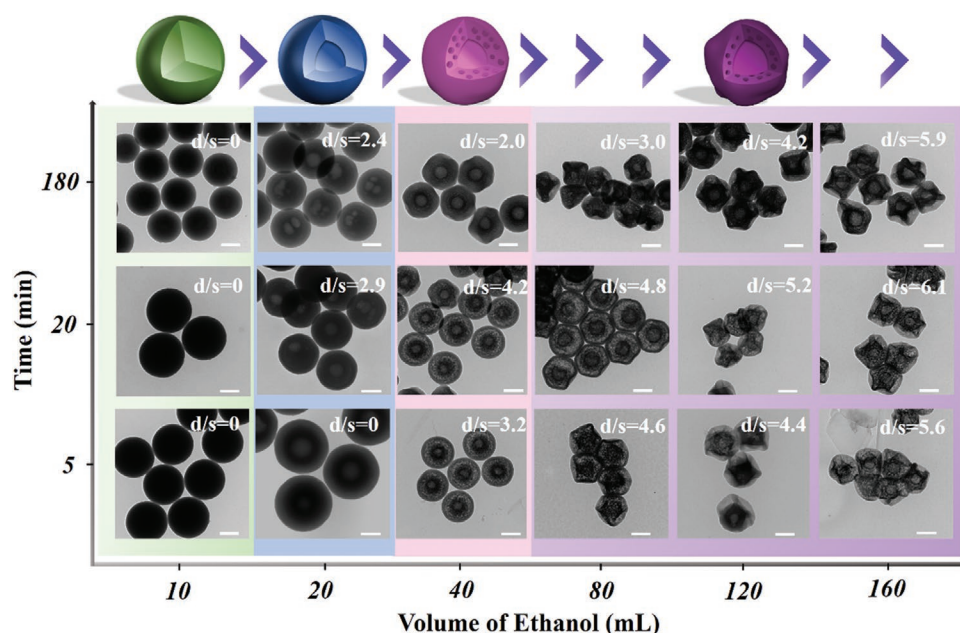
**ADVANCED
SCIENCE NEWS**

www.advancedsciencenews.com

**ADVANCED
MATERIALS**

www.advmat.de

Figure 3. TEM images of multilevel structured APF resins with different volume of ethanol and time. Scale bars = 200 nm. The upmost panel shows the 3D model of the corresponding architectures.

2.3. Various Multilevel Hollow Nanomaterials

Previous reports revealed that tuning the ratio of ethanol/water can control the diameters, morphology, and the degree of condensation of polymer nanospheres.[19,28] The evolution process of these special multilevel hollow structures through treatment with different volumes of ethanol, with time was studied (**Figure 3**; Figure S9, Supporting Information). When 10 mL ethanol was used, no matter how long it was treated, the APF maintained its complete spherical structure without obvious etching. By increasing the volume of ethanol to 20 mL, the inner parts of the APF were partially engraved and produced a hollow structure. The nanoarchitecture of the resultant APF was evolved gradually through variation of the ethanol volume from 20 to 40, 80, 120, and 160 mL, eventually, hollow structures with a roughly hexagonal cross section surface were formed. The d/s values for the APF treated by 10, 20, 40, 80, 120, 160 mL ethanol in 180 min were 0, 2.4, 2.0, 3.0, 4.2 and 5.9, respectively. Those phenomena were due to the fast reaction between short-chain oligomers with increasing amounts of ethanol. In addition, the structure changes with time were carried out, the ratio of d/s shows the tendency of increase first and then decrease, to identify the dissolution and repolymerization mechanism again. Meanwhile, the ^{13}C CP/MAS spectra of the APF treated with 20 and 80 mL of ethanol for 20 and 180 min were also displayed in Figure S10 (Supporting Information). Because of the low amount of ethanol, for APF-20, the peak area ratio of aromatic C/alkylated C changed slightly, while APF-80 exhibited an increased tendency with almost the same phenomenon observed in APF-40.

Moreover, the dissolution effect on APF is influenced by the different dissolving capability of the solvents toward oligomer species. Therefore, in addition to ethanol, four more types of alcohol (including methanol, glycol, isopropanol, and glycerol)

with different engraving effects on APF have been explored. The APF maintained its original sphere structure without obvious pores in methanol (Figure S11a, Supporting Information). A relatively higher etching degree for APF with porous nanosphere structure could be obtained by the use of glycol and glycerol (Figure S11b,c, Supporting Information). Instead of maintaining typical nanospheres, the nanoparticle with roughly hexagonal cross-section could be observed when applied isopropanol as the etchant, whose dissolving effect is similar with ethanol (Figure S11d, Supporting Information). Such knowledge of the nanoscale chemical surgery can be applicable to other resin materials prepared with suitable precursors. For example, RF and RF/APF resin materials with similar multilevel hollow nanostructures were successfully obtained (Figure S12a,b, Supporting Information). The STEM and EDX elemental mapping images for RF/APF resin clearly exhibited this structure and uniformly distributed C, O, N elements (Figure S12c, Supporting Information). However, when *m*-phenylenediamine was chosen to react with formaldehyde, the same unique nanostructure was not successfully formed, instead of uneven spherical morphology, which is probably attributed to the unsuccessful formation of resin spheres with different polymerization degrees (Figure S12d, Supporting Information).

2.4. Bimetallic Nanoreactors and Catalytic Hydrogenation Performance

Engineering nanomaterials toward hollow architectures and special compositions can enable them to accurately locate metal nanoparticles. Simultaneously, an in-depth understanding of the influence of structural changes of APF on position and distribution of metal nanoparticles (such as AuNPs) can reveal some important internal structure and composition characteristics
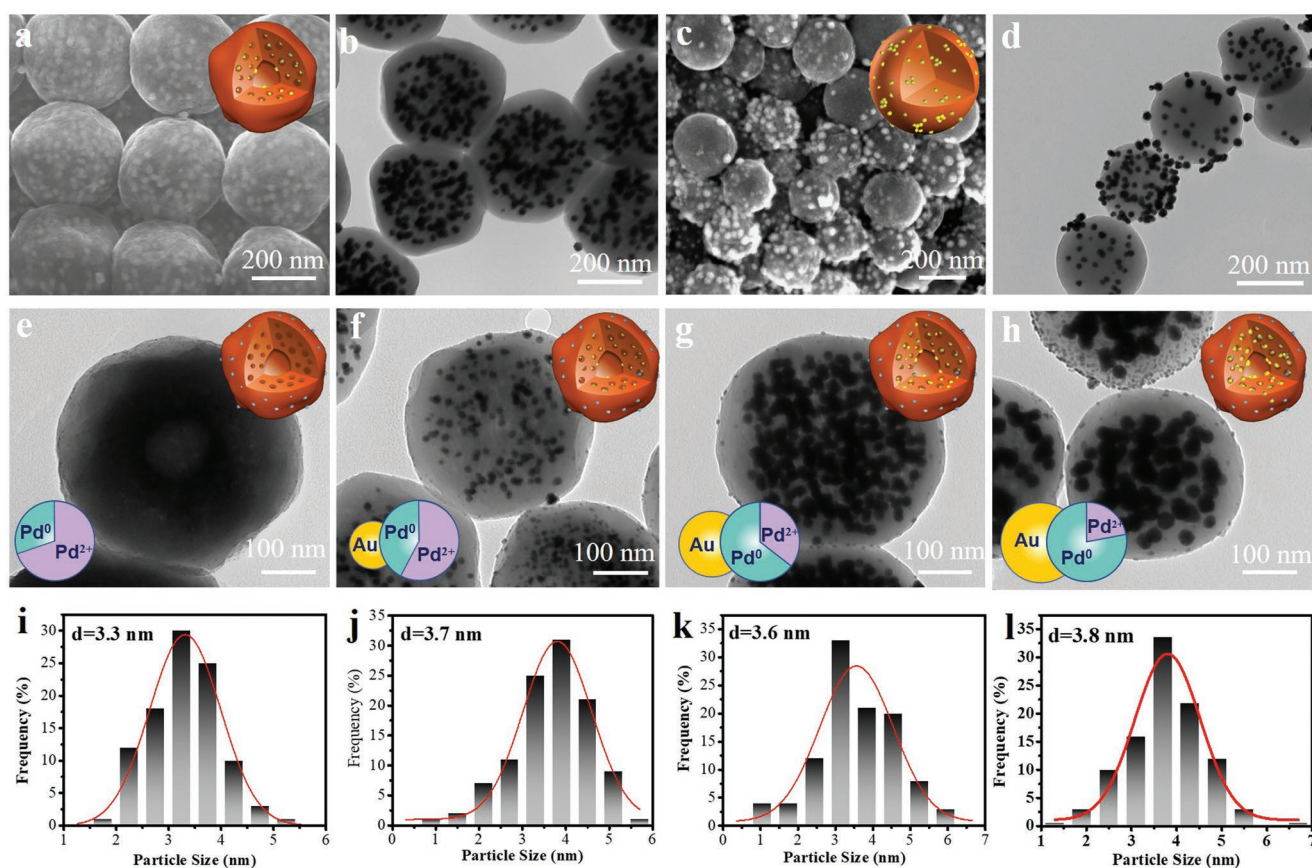
**ADVANCED
SCIENCE NEWS**

www.advancedsciencenews.com

**ADVANCED
MATERIALS**

www.advmat.de

Figure 4. a) HRSEM and b) TEM images of Au@APF-40-180-2. c) SEM and d) TEM images of Au@Solid APF-2. TEM images of e) APF-40-180@Pd, f) Au@APF-40-180-1@Pd, g) Au@APF-40-180-2@Pd, and h) Au@APF-40-180-3@Pd. i–l) The size distribution histogram of the corresponding Pd nanoparticle (the size distribution of Pd nanoparticle size is obtained from TEM images analysis by using at least 100 nanoparticles).

of APF. Important structural elements are: 1) the hydroxymethyl groups, reducing Au^{3+} to AuNPs; 2) the amine groups, influence the penetration depth of $HAuCl_4$ and the position of AuNPs; and, 3) abundant pores, providing space microenvironment for the location of AuNPs.[49] From the HRSEM (**Figure 4**a), and TEM (Figure 4b) images, we can see that the Au@APF-40-180-2 composite had smooth and uniform surfaces. AuNPs did not appear on the surface of APF-40-180 but were homogeneously and fully inserted inside of the resin spheres. Whether decreasing (Figure S13a,c, Supporting Information) or increasing (Figure S13b,d, Supporting Information) the $HAuCl_4$ concentration, AuNPs did not appear on the surface of APF-40-180 but were embedded inside of the APF resin spheres. Besides, APF-40-180 particles have the ability to reduce Au^{3+}; the other nanostructured APF resins, such as APF-40-20 and APF-120-180 can reduce Au^{3+} to AuNPs with most of Au incorporated in the APF resins (Figure S14a,b, Supporting Information). In order to further illustrate the importance of amino groups in confining AuNPs, we designed an amine-free hollow RF as carrier to load AuNPs, as displayed in Figure S14c (Supporting Information). The AuNPs obtained inhomogeneous particle size and dispersed randomly around the resins. Therefore, it is very clear to conclude that amine groups mainly affect the particle size and position of AuNPs. Meanwhile, the Au@Solid APF samples with the same

adding amount of $HAuCl_4$ were also shown for comparison (Figure 4c,d; Figure S15, Supporting Information). Remarkably, the AuNPs unevenly dispersed throughout the Solid APF, and parts of those AuNPs localized on the surface of resin spheres, trended to aggregate. The thermogravimetric (TG) profiles were also shown in Figure S16 (Supporting Information), indicating that the Au loading amount for Solid APF is similar with APF-40-180. These phenomena illustrated that benefiting from the alcoholic-assisted dissolution and repolymerization process, the inner parts of the obtained APF-40-180 resins are porous, possess a high density of hydroxymethyl groups ($Ar-CH_2OH$) and amine groups ($-NR(H)$), which are conducive to the accurate positioning of AuNPs.

These uniquely structured Au@APF-40-180 composites not only pave the way toward novel nanoreactors, but also provide platforms to design new Au-based catalysts with customizable catalytic components. After selective depositing Pd nanoparticles on the outer shell of Au@APF-40-180, the as-prepared samples were characterized by TEM (Figure 4e–h), Pd nanoparticles were successfully deposited onto APF-40-180 and Au@APF-40-180. The average Pd nanoparticle sizes in all of those samples were almost the same (Figure 4i–l). From what has been discussed above, we can infer that the spatial location of metal nanoparticle is closely related to the matrix properties and experimental methods. Inner parts of APF-40-180

ADVANCED
SCIENCE NEWS
www.advancedsciencenews.com

ADVANCED
MATERIALS
www.advmat.de

resins are porous, which can provide sufficient diffusion channel for $HAuCl_4$ molecule and chemical microenvironment for loading AuNPs inside them. Furthermore, abundant amine groups ($-NR(H)$) and reducing groups (hydroxymethyl groups) are effective for anchoring and reduction of Au^{3+} to precisely located AuNPs. Moreover, the reducing capacity of the hydroxymethyl groups is not sufficient to reduce Pd^{2+} to form PdNPs (Figure S17, Supporting Information).[50,51] Therefore, our developed method is very effective for spatial location controllable synthesis of AuNPs and PdNPs, selectively. We also investigated the inductively coupled palsma optical emission spectroscopy (ICP-OES) (Table S2, Supporting Information) and X-ray diffraction (XRD) (Figure S18, Supporting Information) for those bimetallic nanomaterials, whose detailed analyses are shown in the supporting information. The X-ray photoelectron spectroscopy (XPS) results of those Au@APF-40-180@Pd with different amounts of Au were shown in Figure S19 (Supporting Information). The Pd 3d spectra of those samples contained four deconvoluted peaks with binding energies of 333.9, 336.5, 339.1, and 341.8 eV. The doublet peaks at 333.9 and 339.1 eV belong to the $Pd\ 3d_{5/2}$ and $Pd\ 3d_{3/2}$ states of Pd^0, respectively.[52] The other doublet peaks are assigned to Pd^{2+}.[53] Obviously, with the increase of Au, the percentage of Pd^0 show a trend of increase (Figure S19a, Supporting Information). In addition, the Au 4f spectra were shown in Figure S19b (Supporting Information). All the AuPd bimetallic samples showed the same spectra with two peaks at around 84 and 88 eV, which were assigned to Au $4f_{7/2}$ and Au $4f_{5/2}$ electrons of Au metal, respectively.[54,55] The Au $4f_{7/2}$ spectra of AuPd bimetallic samples showcased the shift of binding energy toward higher values with the addition of more Au. Both the increased percentage of Pd^0 and the positive shifts for Au 4f could be attributed to the electron transfer between Pd and Au.

High angle annular dark fields STEM (HAADF-STEM) image of Au@APF-40-180-3@Pd showed clearly that AuNPs were fully embedded into the resin spheres with a distance of ≈40 nm from the exterior surface, and PdNPs homogenously dispersed on those Au@APF composites (**Figure 5**a). The catalytic performances of those obtained bimetallic catalysts were first evaluated in the hydrogenation of styrene at 40 °C and 1 bar H_2 (Figure 5b). It was found that monometallic Au and Pd on APF show negligible catalytic activities for styrene hydrogenation with the conversion of only 0.1 and 1%, respectively, after 120 min. However, with introducing Pd into the Au@APF composites to form AuPd bimetallic catalysts, those catalysts show markedly enhanced hydrogenation performance. Moreover, with the increase of Au amount, the catalysts exhibited a much higher activity. In addition, varying the S/C from 50 to 500 could obtain the optimal conversion (Figure S20, Supporting Information). The diffusion behavior of styrene could affect the reaction time rather than intrinsic activity. In addition, in the phenylacetylene hydrogenation reactions, these catalysts showed similar experimental results (Figure 5c). With respect to the bare AuNPs and PdNPs supported on

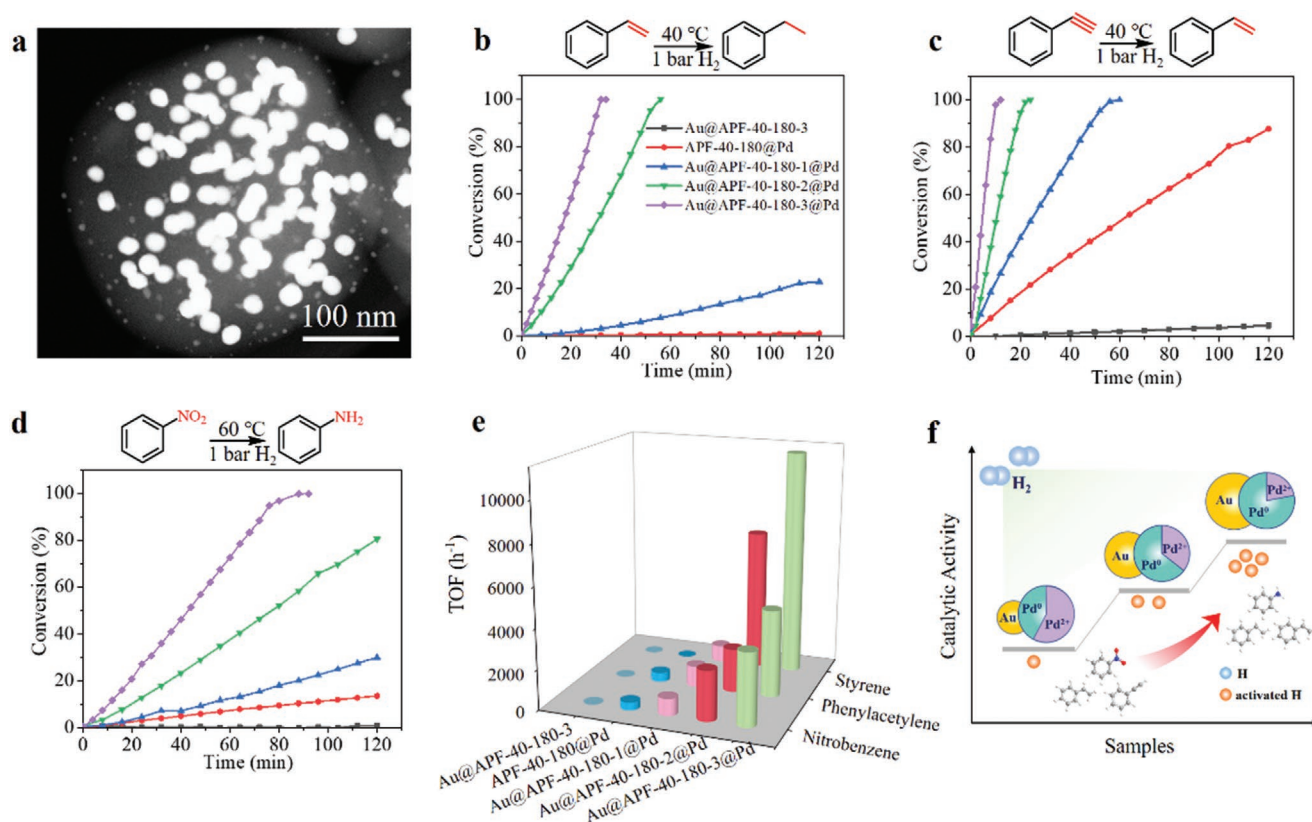**Figure 5.** a) HAADF-STEM image of Au@APF-40-180-3@Pd, and catalytic activity in hydrogenation of b) styrene, c) phenylacetylene, and d) nitrobenzene. e) The corresponding TOF values of different catalysts in styrene, phenylacetylene, and nitrobenzene hydrogenations. f) Scheme of the increased activities among different bimetallic catalysts.

APF-40-180, the bimetallic catalysts display significantly enhanced catalytic efficiency.

We also employed nitrobenzene as the substrate to explore the hydrogenation performance of those Au@APF-40-180@Pd catalysts (Figure 5d). Therein, similar experimental results could be obtained. First, monometallic Au@APF was totally inactive. Although the monometallic Pd@APF demonstrates limited hydrogenation reaction performance, the conversion was extremely lower than that AuPd bimetallic catalysts. Au@APF-40-180@Pd exhibited excellent catalytic activity and selectivity for the hydrogenation of nitroarenes to produce the corresponding aniline (>99%). The TOF values of those catalysts employed in various reactions were summarized in Figure 5e. In the hydrogenation of styrene, Au@APF-40-180-3@Pd showed highest TOF value of 11257 h^{-1}, which was more than 1.6 and 13 times higher than those Au@APF-40-180-2@Pd (7030 h^{-1}) and Au@APF-40-180-1@Pd (828 h^{-1}), respectively. Similarly, for the phenylacetylene and nitrobenzene hydrogenation, the TOF value gradually increased by embedding more AuNPs. Among the Au@APF-40-180@Pd catalysts with different Au amounts, the Au@APF-40-180-3@Pd exhibited the highest hydrogenation catalytic activity, which can be attributed to the higher amount of Pd^0 in this catalyst. For comparison, we also summarized the related results of state-of-the-art catalysts reported in the literature (Table S3, Supporting Information). The Au@APF-40-180-3@Pd displayed extraordinary catalytic activities, which have proved to be superior among most of the reported results. The stability test of Au@APF-40-180-3@Pd was carried out in the styrene hydrogenation. The catalyst can be recycled for five times without considerable changes in the activity (Figure S21a, Supporting Information). Moreover, the spent nanocatalyst after five runs maintained its original structure, which could confirm the excellent stability of the bimetallic catalyst (Figure S21b, Supporting Information). Every component in our designed catalyst coordinated to achieve high-efficiency hydrogenation performance. The encapsulated AuNPs were favorable for supplying electron to PdNPs accompanied by more metallic Pd formation. Moreover, PdNPs on the outer shell favored more activated hydrogen available for the activation of substrates. Because of the existence of synergistic effect between Au and Pd, when the nanocatalyst decorated with more AuNPs, the PdNPs would be enriched with high percentage of Pd^0 to favorably active H_2, and enhance the catalytic efficiency thereafter (Figure 5f).

3. Conclusion

In summary, we demonstrated a unique "top-down" strategy based on the dissolution and repolymerization process, nanoscale chemical surgery, to precisely tailor the nanostructure and chemical composition of the phenolic resin spheres at nanoscale. This strategy relies on the use of chemical scissors, ethanol, to selectively cleave the chemical bonds (Ar(C)—N bonds), followed by a repolymerization process, the Solid APF spheres transformed to multilevel hollow structure with Ar—CH$_2$OH and —NR(H) uniformly distributed inside those materials. The unique nanoarchitectures and their organic microenvironments provided the opportunity to precisely localize multiple AuNPs within one single APF resin. Furthermore, after deposition of Pd onto the surface of those Au@APF composites, the resulting AuPd bimetallic catalysts are promising in the hydrogenation of styrene, phenylacetylene, and nitrobenzene (the highest TOF value = 11257 h^{-1} in the styrene hydrogenation). We believe the chemical surgery process demonstrated in this work provides new platform for custom, complex hollow architectures and sophisticated catalysts with precise spatial active components. Finally, we look forward to the nanoreactor with precise spatial positioning of metal nanoparticles. The controllable structure for this nanoreactor, containing well-known plasmonic metal, AuNPs, is significant for modulating and optimizing the plasmonic coupling and the formation of hot spots. After customizing with different catalytic components, PdNPs, the designated AuPd bimetallic nanoreactor may have great prospect in sustainable solar light induced reactions, such as "Suzuki–Miyaura cross-coupling" and "alkynyl annulation", alcohol oxidation.

4. Experimental Section

Preparation of APF: In a typical synthesis, 3-aminophenol (3-AP, 0.1 g), formaldehyde solution (HCHO, 37 wt.%, 0.1 mL), and ammonia aqueous solution (NH$_4$OH, 25 wt.%, 0.1 mL) as a catalyst were added into deionized water (30 mL) and reacted at 30 °C. After the reaction continued for 30 min, ethanol with different volume X (X = 10, 20, 40, 80, 120, 160 mL) was added. At a certain reaction time Y (Y = 5, 20, 180 min), the APF-X-Y was obtained by centrifugal and washed with deionized water. After centrifugation, the product was dried for 24 h in 30 °C vacuum oven. For the preparation of Solid APF, the resin spheres were collected after reaction for 30 min, instead of treating with ethanol.

The detailed experimental procedure of APF synthesized with H$_2$O–ethanol binary solvents was as follows: 3-aminophenol (3-AP, 0.1 g) was dissolved in H$_2$O (30 mL) and ethanol (40 mL) solvents at 30 °C. Afterward, formaldehyde solution (HCHO, 37 wt.%, 0.1 mL), and ammonia aqueous solution (NH$_4$OH, 25 wt.%, 0.1 mL) were added into that solution and kept stirring for 180 min. After centrifugation, washing with deionized water and drying in a vacuum oven, the final product was obtained.

The synthesis processes of APF treated by different types of alcohols were almost the same as APF-40-180, except for replacing ethanol with methanol, glycol, isopropanol, and glycerol, respectively.

Preparation of Au@APF: In a typical procedure, APF-40-180 obtained from centrifugation were dispersed in water (30 mL) and stirred by simple magnetic at 70 °C. Afterward, HAuCl$_4$ aqueous solution (5 mL) of 4.9, 24, and 97 mM were added into the above solution dropwise, respectively. After 10 min, the obtained Au@APF-40-180-Z (Z = 1, 2, 3 represents the changes of HAuCl$_4$ concentration) were obtained by centrifugal and washed by deionized water three times. After centrifugation, the product was dried for 12 h in 60 °C oven. The preparation method and Au loading amounts of Au@Solid APF were the same as that of Au@APF-40-180. Au@APF-40-20 and Au@APF-120-180 were the same as that of Au@APF-40-180-1.

Preparation of Au@APF-40-180@Pd: In a typical synthesis, PdCl$_2$ (0.02 mol L^{-1}, 0.94 mL) and citric acid (44 mg) were dissolved in water (50 mL) to form Pd–citric solution. Followed by adding Au@APF-40-180-Z (Z = 1, 2, 3) (40 mg) and sonicating for 20 min. After that, the desired amount of NaBH$_4$ solution (0.016 mol L^{-1}, 10 mL) was added into the above mixture and stirred for 4 h at 60 °C. Then the resulting products were collected by filtrating, washed with deionized water, and finely dried at 60 °C overnight.

Catalytic Performance Evaluation: The hydrogenation reaction was carried out in a three-necked round-bottom flask (100 mL capacity). For styrene hydrogenation, a given amount of solid catalyst (10 mg) was

**ADVANCED
SCIENCE NEWS**

www.advancedsciencenews.com

**ADVANCED
MATERIALS**

www.advmat.de

placed in the flask, then added styrene (9.6 mmol) and ethanol (15 mL). In order to remove the air, the flask was charged with H_2 for ≈ 1 min at the flow of 50 mL min^{-1}. After that, the reactor was heated to 40 °C with vigorous stirring at 500 rpm. The reaction product was identified and quantified by a Shimadzu GC-2014 gas chromatography equipped with an AT-FFAP chromatographic column, an auto-injector, and a flame ionization detector (FID). In the hydrogenation of nitrobenzene, the reaction temperature and S/C were 60 °C and 100, respectively. Otherwise, in the phenylacetylene hydrogenation reaction, the reaction temperature and S/C were 40 °C and 10, respectively.

The formula for calculating the TOF was as follows:

$$TOF = \frac{n_{sub} \times Conv._{sub}}{n_{Pd} \times D \times t} \tag{1}$$

Here, n_{sub} and n_{Pd} refer to the substrate and Pd moles, respectively. Conv.$_{sub}$ (= 20%) is the conversion of substrate after reaction. D is the dispersion of Pd and t is the reaction time in hours.

Characterization: The scanning electron microscopy (SEM) was detected on FEI Quanta 200F scanning electron microscope operating at an acceleration voltage of 20 kV. High-resolution scanning electron microscopy (HRSEM) images were recorded on a Hitachi S5500 with a point resolution of 0.40 nm operating at 30 KV. The transmission electron microscopy (TEM) was acquired using a Hitachi HT-7700 at an acceleration voltage of 100 kV. High-resolution scanning transmission electron microscopy (HRSTEM) and energy-dispersive X-ray spectroscopy (EDX) images were recorded on JEOL JEM-F200. The sample morphology was also characterized by the aberration-corrected high-angle annular dark fields scanning transmission electron microscopy (HAADF-STEM, JEM-ARM200F). Au and Pd loading amounts of all the samples were collected by inductively coupled plasma optical emission spectroscopy (ICP-OES, ICPS-8100, Shimadzu). Fourier transform infrared (FTIR) spectra were carried on Nicolet iS50. The powder X-ray diffraction data were collected on a Smart Lab diffractometer with Cu Kα radiation (λ = 1.5418 Å) over the 2θ range of 10–90° with a scan speed of 20° min^{-1} at room temperature. N_2 adsorption isotherms were undertaken on a Micromeritics ASAP 2460 instrument. Thermogravimetric Analysis (TGA) was conducted on a PerkinElmer TGA4000. All the solid-state nuclear magnetic resonance (ssNMR) experiments were carried out on a Bruker Avance III600 MHz spectrometer with a 3.2 mm DVT MAS prove with a spinning rate of 20 kHz. For all the ^{13}C cross-polarization experiments, the contact time of 1.5 ms and pulse delay of 2 s was applied. X-ray photoelectron spectroscopy (XPS) was performed on a Thermofisher Excalab X+ spectrometer with Al Kα X-ray radiation source (hν = 1486.6 eV). Matrix-Assisted Laser Desorption/Ionization-Time of Flight (MALDI-TOF) mass spectrometry (MS) was measured by MALDI-TOF/TOF 5800.

Supporting Information

Supporting Information is available from the Wiley Online Library or from the author.

Acknowledgements

Conflict of Interest

The authors declare no conflict of interest.

Data Availability Statement

The data that support the findings of this study are available in the supplementary material of this article.

Keywords

[1] T. Takeichi, T. Kawauchi, T. Agag, *Polym. J.* **2008**, *40*, 1121.
[2] M. Weber, M. Weber, *Phenolic Resins: A Century of Progress*, Springer, Berlin **2010**.
[3] Z.-Y. Ma, Z.-L. Yu, Z.-L. Xu, L.-F. Bu, H.-R. Liu, Y.-B. Zhu, B. Qin, T. Ma, H.-J. Zhan, L. Xu, H.-A. Wu, H. Ding, S.-H. Yu, *Matter* **2020**, *2*, 1270.
[4] Y. Shiraishi, T. Takii, T. Hagi, S. Mori, Y. Kofuji, Y. Kitagawa, S. Tanaka, S. Ichikawa, T. Hirai, *Nat. Mater.* **2019**, *18*, 985.
[5] S.-R. Guo, J.-Y. Gong, P. Jiang, M. Wu, Y. Lu, S.-H. Yu, *Adv. Funct. Mater.* **2008**, *18*, 872.
[6] Chen, X. , *Science* **2002**, *295*, 1698.
[7] M. Oh, C. A. Mirkin, *Nature* **2005**, *438*, 651.
[8] Z. Min, S. Hao, Y. Yang, X. Huang, C. Yu, *Angew. Chem., Int. Ed.* **2018**, *57*, 654.
[9] H. Tian, J. Liang, J. Liu, *Adv. Mater.* **2019**, *31*, 1903886.
[10] A. S. Aricò, P. Bruce, B. Scrosati, J.-M. Tarascon, W. Van Schalkwijk, *Nat. Mater.* **2005**, *4*, 366.
[11] C. Gao, F. Lyu, Y. Yin, *Chem. Rev.* **2021**, *121*, 834.
[12] L. Peng, H. Peng, C.-T. Hung, D. Guo, L. Duan, B. Ma, L. Liu, W. Li, D. Zhao, *Chem* **2021**, *7*, 1020.
[13] Y. Zhao, L. Jiang, *Adv. Mater.* **2009**, *21*, 3621.
[14] Z. Xiong, B. Sun, H. Zou, R. Wang, Q. Fang, Z. Zhang, S. Qiu, *J. Am. Chem. Soc.* **2022**, *144*, 6583.
[15] L. Peng, H. Peng, Y. Liu, X. Wang, C.-T. Hung, Z. Zhao, G. Chen, W. Li, L. Mai, D. Zhao, *Sci. Adv.* **2021**, *7*, eabi7403.
[16] K. Li, Y. Zhao, J. Yang, J. Gu, *Nat. Commun.* **2022**, *13*, 1879.
[17] H. Qiu, Z. M. Hudson, M. A. Winnik, I. Manners, *Science* **2015**, *347*, 1329.
[18] H. Qiu, G. Yang, V. A. Du, R. Harniman, M. A. Winnik, I. Manners, *J. Am. Chem. Soc.* **2015**, *137*, 2375.
[19] J. Liu, S. Z. Qiao, H. Liu, J. Chen, A. Orpe, D. Zhao, G. Q. Lu, *Angew. Chem., Int. Ed.* **2011**, *50*, 5947.
[20] J. Zhao, W. Niu, L. Zhang, H. Cai, M. Han, Y. Yuan, S. Majeed, S. Anjum, G. Xu, *Macromolecules* **2013**, *46*, 140.
[21] Y. Fang, D. Gu, Y. Zou, Z. Wu, F. Li, R. Che, Y. Deng, B. Tu, D. Zhao, *Angew. Chem., Int. Ed.* **2010**, *49*, 7987.
[22] J. Liu, T. Yang, D.-W. Wang, G. Q. Lu, D. Zhao, S. Z. Qiao, *Nat. Commun.* **2013**, *4*, 2798.
[23] L. Hu, Z. Qian, W. Gao, X. Wang, Y. Tian, *J. Mater. Sci.* **2020**, *55*, 2052.
[24] C. Hou, Y. Wang, Q. Ding, L. Jiang, M. Li, W. Zhu, D. Pan, H. Zhu, M. Liu, *Nanoscale* **2015**, *7*, 18770.
[25] D.-S. Bin, Y.-S. Xu, S.-J. Guo, Y.-G. Sun, A.-M. Cao, L.-J. Wan, *Acc. Chem. Res.* **2021**, *54*, 221.
[26] D. S. Bin, Z. X. Chi, Y. Li, K. Zhang, X. Yang, Y. G. Sun, J. Y. Piao, A. M. Cao, L. J. Wan, *J. Am. Chem. Soc.* **2017**, *139*, 13492.
[27] R. Yu, X. Huang, Y. Liu, Y. Kong, Z. Gu, Y. Yang, Y. Wang, W. Ban, H. Song, C. Yu, *Adv. Sci.* **2020**, *7*, 2000393.

**ADVANCED
SCIENCE NEWS**

www.advancedsciencenews.com

**ADVANCED
MATERIALS**

www.advmat.de

[28] S. Zhou, Y. Bai, W. Xu, J. Feng, X. Wang, Z. Li, Y. Yin, *Nanoscale* **2020**, *12*, 15460.

[29] A. Kumar, N. Kumari, S. Dubbu, S. Kumar, T. Kwon, J. H. Koo, J. Lim, I. Kim, Y.-K. Cho, J. Rho, I. S. Lee, *Angew. Chem., Int. Ed.* **2020**, *59*, 9460.

[30] K. Ariga, *Small Sci.* **2021**, *1*, 2000032.

[31] J. Liu, Z. Guo, K. Liang, *Adv. Funct. Mater.* **2019**, *29*, 1905321.

[32] C. Dong, Q. Yu, R.-P. Ye, P. Su, J. Liu, G.-H. Wang, *Angew. Chem., Int. Ed.* **2020**, *59*, 18374.

[33] W. Zang, G. Li, L. Wang, X. Zhang, *Catal. Sci. Technol.* **2015**, *5*, 2532.

[34] X. Ren, M. Guo, H. Li, C. Li, L. Yu, J. Liu, Q. Yang, *Angew. Chem., Int. Ed.* **2019**, *58*, 14483.

[35] H. Zou, J. Dai, J. Suo, R. Ettelaie, Y. Li, N. Xue, R. Wang, H. Yang, *Nat. Commun.* **2021**, *12*, 4968.

[36] L. Luo, W.-S. Lo, X. Si, H. Li, Y. Wu, Y. An, Q. Zhu, L.-Y. Chou, T. Li, C.-K. Tsung, *J. Am. Chem. Soc.* **2019**, *141*, 20365.

[37] K. Choe, F. Zheng, H. Wang, Y. Yuan, W. Zhao, G. Xue, X. Qiu, M. Ri, X. Shi, Y. Wang, G. Li, Z. Tang, *Angew. Chem., Int. Ed.* **2020**, *59*, 3650.

[38] Y.-F. Jiang, C.-Z. Yuan, X. Xie, X. Zhou, N. Jiang, X. Wang, M. Imran, A.-W. Xu, *ACS Appl. Mater. Interfaces* **2017**, *9*, 9756.

[39] C. Chen, W. Ou, K.-M. Yam, S. Xi, X. Zhao, S. Chen, J. Li, P. Lyu, L. Ma, Y. Du, W. Yu, H. Fang, C. Yao, X. Hai, H. Xu, M. J. Koh, S. J. Pennycook, J. Lu, M. Lin, C. Su, C. Zhang, J. Lu, *Adv. Mater.* **2021**, *33*, 2008471.

[40] X. Li, Y. Pan, H. Yi, J. Hu, D. Yang, F. Lv, W. Li, J. Zhou, X. Wu, A. Lei, L. Zhang, *ACS Catal.* **2019**, *9*, 4632.

[41] H. Tian, F. Huang, Y. Zhu, S. Liu, Y. Han, M. Jaroniec, Q. Yang, H. Liu, G. Q. M. Lu, J. Liu, *Adv. Funct. Mater.* **2018**, *28*, 1801737.

[42] K. F. Kelton, *Solid State Physics*, Academic Press, Cambridge, **1991**.

[43] G.-P. Hao, W.-C. Li, D. Qian, G.-H. Wang, W.-P. Zhang, T. Zhang, A.-Q. Wang, F. Schüth, H.-J. Bongard, A.-H. Lu, *J. Am. Chem. Soc.* **2011**, *133*, 11378.

[44] X. Zhang, M. Looney, D. Solomon, A. Whittaker, *Polymer* **1997**, *38*, 5835.

[45] D. J. Allen, H. Ishida, *Polymer* **2007**, *48*, 6763.

[46] J. M. García, G. O. Jones, K. Virwani, B. D. Mccloskey, D. J. Boday, G. M. Ter Huurne, H. W. Horn, D. J. Coady, A. M. Bintaleb, A. M. S. Alabdulrahman, F. Alsewailem, H. a. A. Almegren, J. L. Hedrick, *Science* **2014**, *344*, 732.

[47] A. Chernykh, J. Liu, H. Ishida, *Polymer* **2006**, *47*, 7664.

[48] J. Zhao, M. R. H. S. Gilani, J. Lai, A. Nsabimana, Z. Liu, R. Luque, G. Xu, *Macromolecules* **2018**, *51*, 5494.

[49] M. K. Khan, M. J. Maclachlan, *ACS Macro Lett.* **2015**, *4*, 1351.

[50] B. Pal, P. K. Sen, K. K. Sen Gupta, *J. Phys. Org. Chem.* **2001**, *14*, 284.

[51] X. Yin, J. Yang, M. Zhang, X. Wang, W. Xu, C.-a. H. Price, L. Huang, W. Liu, H. Su, W. Wang, H. Chen, G. Hou, M. Walker, Y. Zhou, Z. Shen, J. Liu, K. Qian, W. Di, *ACS Nano* **2022**, *16*, 2852.

[52] Z. Tian, C. Dong, Q. Yu, R.-P. Ye, M. S. Duyar, J. Liu, H. Jiang, G.-H. Wang, *Mater. Today* **2020**, *40*, 72.

[53] M. Li, Z. Xia, M. Luo, L. He, L. Tao, W. Yang, Y. Yu, S. Guo, *Small Sci.* **2021**, *1*, 2100061.

[54] H. Tian, J. Zhao, X. Wang, L. Wang, H. Liu, G. Wang, J. Huang, J. Liu, G. Q. Lu, *Natl. Sci. Rev.* **2020**, *7*, 1647.

[55] Y. Hong, V. Rozyyev, C. T. Yavuz, *Small Sci.* **2021**, *1*, 2000078.